

Evidence of the fast acceleration of AGN-driven winds at kiloparsec scales

Received: 18 July 2024

Accepted: 26 February 2025

Published online: 31 March 2025

 Check for updates

Cosimo Marconcini  ^{1,2}✉, Alessandro Marconi  ^{1,2}, Giovanni Cresci  ², Filippo Mannucci  ², Lorenzo Ulivi  ^{1,2,3}, Giacomo Venturi  ^{2,4}, Martina Scialpi  ^{1,2,3}, Giulia Tozzi  ⁵, Francesco Belfiore  ², Elena Bertola  ², Stefano Carniani  ⁴, Elisa Cataldi ^{1,2}, Avinanda Chakraborty ², Quirino D'Amato  ², Enrico Di Teodoro ^{1,2}, Anna Feltre  ², Michele Ginolfi  ^{1,2}, Bianca Moreschini  ^{1,2}, Nicole Orientale  ^{1,2}, Bartolomeo Trefoloni  ^{1,2} & Andrew King ^{6,7,8}

Supermassive black holes at the centres of galaxies gain mass through accretion disks. Different models predict that quasi-spherical winds, expelled by black holes during accretion, have a key role in galaxy evolution through regulating star formation and the distribution of metals over kiloparsec scales and sweeping ambient gas to the outskirts of galaxies. Nonetheless, the mechanism that drives these outflows and the amount of energy exchanged between the wind and the galaxy's interstellar medium remain unclear. Here we analyse the kinematic properties of these winds in a sample of nearby active galaxies using the MOKA^{3D} model, which reproduces the clumpy nature of the interstellar medium. We provide evidence that outflows exhibit a regular radial velocity trend—initially constant or slightly decreasing, followed by rapid acceleration starting at approximately 1 kpc from the nucleus—despite the seemingly complex kinematics. The observed behaviour is consistent with current theoretical understanding of active galactic nucleus outflows, where a momentum-driven phase transitions to an energy-conserving phase beyond 1 kpc. The constant velocity of the momentum-driven wind is then rapidly accelerated following inefficient Compton cooling of post-shock material. The measured radial terminal velocities of the outflows are larger than the escape velocities from the host galaxies, confirming the role of outflows in shaping galaxy evolution as a manifestation of active galactic nucleus feedback.

Multi-wavelength observations of active galactic nuclei (AGN) powered by the accretion of matter onto supermassive black holes (SMBHs) have revealed the presence of multi-phase winds, observed from parsec scales in X-rays ($V_{\text{out}} \approx 0.1c$, where V_{out} is velocity and c is the velocity of light) to kiloparsec scales for molecular, ionized and atomic outflows ($V_{\text{out}} \approx 10^2\text{--}10^3 \text{ km s}^{-1}$) at both low and high redshift^{1–9}. The exact role and impact of these winds in the context of galaxy evolution, the regulation of star formation and, more broadly, their contribution to

feedback mechanisms are still debated and lack a pivotal observational confirmation. Nonetheless, a plethora of observations and theoretical models suggest that during the most intense active phase of AGN in cosmic history, happening at redshift $z \approx 1\text{--}3$, energetic winds propagating through the galaxy quench star formation by ejecting the gas reservoir out of it and by heating the interstellar medium (ISM)^{3–5,10–13}. The mechanisms powering outflows and their energetic impacts on the ISM have not been established; the characterization of the physical

A full list of affiliations appears at the end of the paper. ✉ e-mail: cosimo.marconcini@unifi.it

properties of outflows is therefore crucial to understand how galaxy evolution processes, such as star formation regulation and gas depletion, are ultimately affected by the AGN feedback mechanism.

Outflows are usually detected in the ionized phase by the presence of prominent broad line wings in optical nebular lines, such as [O III] $\lambda\lambda 4959, 5007$ and [N II] $\lambda\lambda 6548, 6584$, mostly tracing warm (temperature $T \approx 10^4$ K) gas ionized by the central AGN^{7,8,14}. Even though nearby, low-luminosity galaxies do not host winds as powerful as those at $z \approx 1-3$, their proximity means that they represent the best candidates to constrain the energy exchange mechanism between AGN-powered phenomena (outflows and jets) and the ISM. During the past decade, our understanding of this mechanism has been improved by spatially resolved, integral field unit observations, which have proved to be essential in providing more comprehensive knowledge of outflow properties. In particular, integral field unit observations of nearby AGN winds allow us to characterize the outflow kinematics and structure in detail from nuclear to galactic scales, taking advantage of spatial resolutions reaching the few-parsec scale for the nearest sources and the high sensitivity that can be achieved¹⁵⁻¹⁸.

To constrain the properties of outflows and galactic disks, it is crucial to adopt a kinematic model that is tailored to account for the complexity of the observed data. The impact of the outflow on the host mainly depends on the amount of carried energy; this is determined by the mass, velocity and extent of the outflowing gas, which are affected by geometrical projection effects and therefore often assumed. The advent of modern ground- and space-based facilities has led to substantial improvements in terms of spatial resolution (for example, refs. 17,19,20). Nevertheless, there are still several uncertainties that affect mass and kinematic measurements.

Most kinematic models rely on assumptions regarding the physical gas properties and, most importantly, are not designed to fully reconstruct the three-dimensional structure of the emitting gas, increasing the uncertainties on the estimated outflow properties (for example, refs. 21-23). As an example, most models assume an analytic smooth gas emissivity, which is an extreme simplification of the clumpy and inhomogeneous emission observed in nearby sources. In such a scenario, the observed complexity of gas emission and kinematics cannot be modelled with simplified models and therefore require a more comprehensive and accurate analysis.

In this Article we apply our 3D kinematic model MOKA^{3D}, presented in ref. 24, to accurately measure the kinematics of ionized AGN-driven outflow in a sample of galaxies selected from the Measuring AGN Under MUSE (MAGNUM) survey^{16,25,26} and listed in Table 1. Our sample is composed of ten Seyfert galaxies with inhomogeneous flux distributions in the ionized outflow regions and complex kinematics, which were difficult to derive reliable kinematic parameters for using standard modelling (see 'Target selection' in the Methods). Indeed, the complexity of the data, together with the limited capabilities of available kinematic models, could only provide coarse estimates of both the velocity and inclination of the outflows. We took advantage of the capabilities of MOKA^{3D} to model this complexity and infer the intrinsic outflow velocity profile, providing a spatially resolved analysis of the outflow geometry and kinematics.

MOKA^{3D} is a 3D kinematic model that allows us to reproduce the clumpy ionized structures observed in spatially resolved data, providing the intrinsic 3D deprojected gas geometry and kinematics (see ref. 24 and the Methods for a more detailed description). To remove the degeneracies that are present when deriving 3D structures from the observed 2D projections on sky, we minimized the numbers of free parameters by considering conical outflows with pure radial velocities: the cones were divided into concentric conical shells and the only free parameters for each shell were the outflow velocity (V_{out}) and inclination with respect the line of sight (β).

As an example of the model capabilities, we discuss the results of the modelling for the nearby Seyfert II galaxy NGC 1365, which has

Table 1 | Properties of the galaxies in the sample

Source	D(Mpc)	$M_{\text{BH}}(\log M_{\odot})$	$M_{\star}(\log M_{\odot})$	$M_{\text{gas}}(\log M_{\odot})$
NGC 4945	3.7	6.15	9.7	9.8
Circinus	4.2	6.54	10.9	9.9
NGC 7582	22.7	7.74	10.5	9.3
Centaurus A	3.8	7.77	9.8	9.4
NGC 1365	18.6	7.30	10.9	10.4
NGC 2992	31.5	7.36	10.8	10.7
IC 5063	45.3	8.24	11.1	9.0
NGC 5643	17.3	6.44	X	X
NGC 5728	44.7	7.53	11.1	9.4
IC 1657	50.5	7.67	10.6	X

The distance (D), SMBH mass (M_{BH}), stellar mass (M_{\star}) and gas mass (M_{gas}) are listed for each source; M_{\odot} is the mass of the Sun. The values for SMBH masses (NGC 4945, ref. 64; Circinus, ref. 65; NGC 7582, ref. 66; Cen A, ref. 67; NGC 1365, ref. 68; NGC 2992, ref. 68; IC 5063, ref. 52; NGC 5643, ref. 69; NGC 5728, ref. 54; IC 1657, ref. 52), stellar masses (NGC 4945, NGC 7582, Cen A, NGC 2992, NGC 1365, IC 5063 and NGC 5728, ref. 70; Circinus, ref. 71; IC 1657, ref. 72) and gas masses (NGC 4945, ref. 73; Circinus, ref. 71; NGC 7582, ref. 74; Cen A, ref. 75; NGC 1365, ref. 77; NGC 2992, ref. 76; IC 5063, ref. 78; NGC 5728, ref. 54) were taken from the literature. 'X' indicates that there were no estimates in the literature; we therefore assumed stellar and gas masses of $10^{10} M_{\odot}$ and $10^{10} M_{\odot}$, respectively, to compute the escape velocity.

already been extensively studied with standard techniques²⁶. From top to bottom, Fig. 1 shows the observed, modelled and residual moment maps, and from left to right the integrated [O III] $\lambda 5007$ emission, line-of-sight velocity and velocity dispersion maps. With MOKA^{3D}, we retrieved the intrinsic (that is, deprojected) velocity profiles of the outflow and disk as a function of the distance from the AGN. Figure 1 shows that we can accurately reproduce the clumpy ionized outflow emission with a conical geometry and a radial velocity field combined with a rotating disk to model the gas emission in the galaxy disk (the same applies to the rest of the sample, see 'MOKA^{3D} fitting and outflow velocity' in the Methods and Supplementary Figs. 4-6).

For this galaxy, we found that the outflow geometry is well reproduced by dispersing clouds in a cone with a total aperture of 120° and average inclination with respect to the line of sight of $81 \pm 10^\circ$. The observed ionized emission is explained by constant radial motions within each conical shell. For this specific galaxy, we divided the outflow in eight concentric shells with a fixed width of $3.8''$. We derived intrinsic radial velocities from -900 km s^{-1} in the inner shell up to $1,500 \text{ km s}^{-1}$ in the outer shell, spanning distances from 0.4 to 2.7 kpc from the AGN.

As a comparison, ref. 26 analysed the ionized gas kinematics of the same source, assuming the peak of the broad component used to fit the line profile as the outflow velocity. With this assumption, and not accounting for projection effects, they found a decelerating outflow velocity profile. In particular, with their assumption they did not account for the broadening of the velocity profile at greater distances, which crucially determines the higher intrinsic outflow velocity. Instead, taking into account projection effects and considering that the outflow physical velocity extends beyond the peak of the broad component (that is, reaching the 1st and 99th percentiles of the line flux), our best-fit model reveals an accelerating profile up to the maximum outflow extension. Finally, Fig. 1 also shows that, despite the observed complex kinematics, the intrinsic velocity field can be explained as a simple radial flow, with the complexity mostly due to the clumpy distribution of ionized clouds (see also ref. 24).

Figure 2 shows the derived radial velocity profiles for all galaxies in the sample (see 'Target selection' in the Methods), normalized to the outflow velocity averaged across the radius within 1 kpc. All galaxies are characterized by a constant or slightly decreasing velocity up to ~ 1 kpc, after which we observed a rapid acceleration in which the outflow radial velocity almost doubles within $\sim 3-5$ kpc. We note that our sample spans a wide range of distances (from ~ 3 Mpc to 50 Mpc), and therefore the

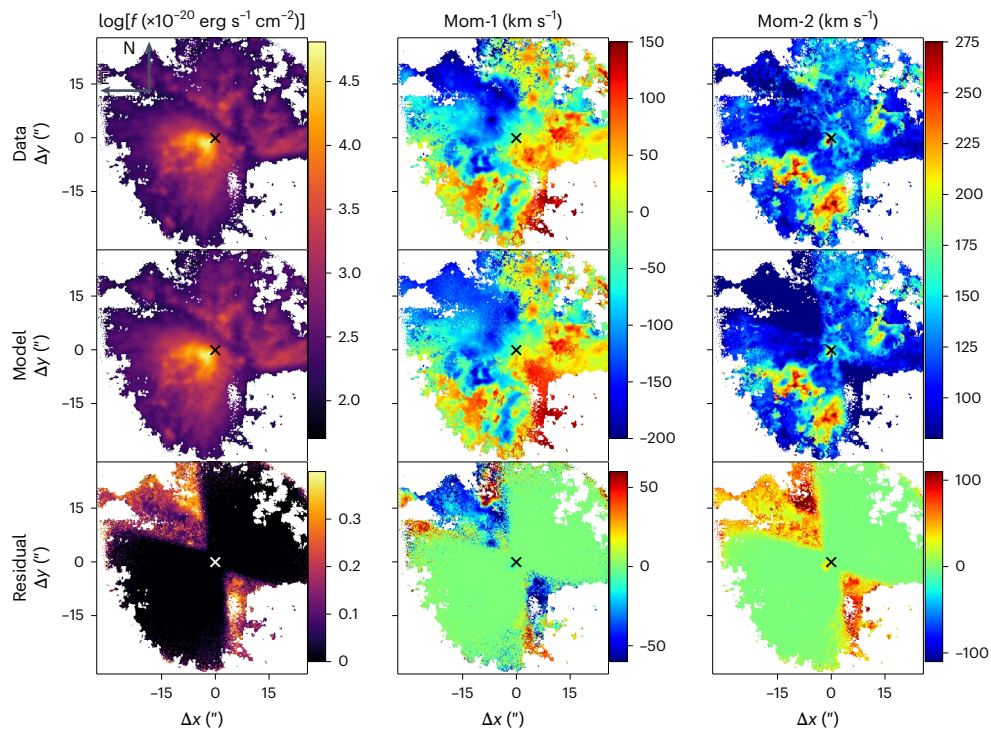


Fig. 1 | Comparison between observed and modelled moment maps for NGC 1365. Observed (top), MOKA^{3D} modelled (middle) and residual (bottom) moment maps are shown for the integrated flux (f ; left), line-of-sight velocity

(MOM-1; middle) and velocity dispersion (MOM-2; right) from [O III] $\lambda 5007$ emission (Methods). The crosses mark the position of the outflow centre. North is up and east is to the left.

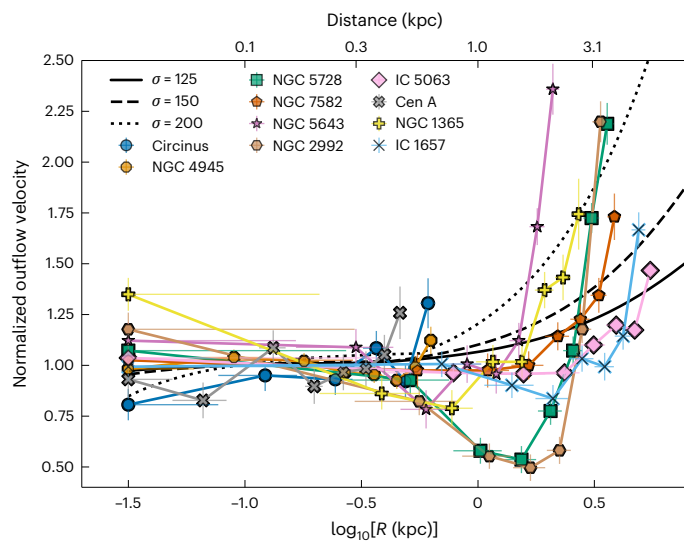


Fig. 2 | Intrinsic outflow radial velocity profile as a function of the distance from the AGN in logarithmic scale. The coloured data points represent the best-fit values of the radial velocity in each shell inferred with MOKA^{3D}. The outflow velocity profiles, as well as their uncertainties, are normalized to the mean outflow velocity within 1 kpc of the AGN. The derivation of the outflow velocities uncertainties is presented in Supplementary Section 3. Error bars represent 1σ uncertainties computed using Supplementary Equation (2). Solid, dashed and dotted black lines represent the trends predicted by the model of ref. 30 assuming stellar velocity dispersions (σ) of 125, 150 and 200 km s^{-1} , $M_{\text{BH}} = 10^8 \text{ M}_{\odot}$ and that the AGN-driven outflow is sustained for 10^7 yr. Details of the model predictions are presented in Supplementary Section 2.

similarities in the radial velocity profiles are not related to the apparent angle projected on the sky. Indeed, in Circinus, NGC 4945 and Cen A (that is, the nearest sources), the observed field of view is not wide

enough to encompass the 1 kpc scale. In these three nearby galaxies ($D \leq 4$ Mpc), we measured a constant average outflow velocity up to their maximum extension, consistent with the other targets. Considering the results for the whole sample, the radial velocity trend suggests that the outflow accelerates at an average distance from the central engine of ~1 kpc, leading to an increase in the radial velocity of up to a factor of ~2. The mean properties of the outflow and disk kinematics and geometry, averaged across different shells, are summarized in Table 2, together with the numbers of shells used.

The simple theoretical model of ref. 27 states that an expanding bubble, driven by the nuclear wind, interacts with the host ISM and generates shocks. Whether the gas shocked by the approaching wind is able to cool efficiently or not will then determine whether the expanding bubble is in a momentum- or energy-conserving phase, respectively. Therefore, the cooling efficiency of the shocked gas has an important influence on the velocity of the outflowing gas shells. Assuming inverse Compton cooling as the most common cooling process^{28,29}, the gas is expected to experience an isothermal momentum-conserving phase with constant velocity followed by an acceleration when transitioning to the energy-conserving phase. When the wind reaches a critical radius of ~1 kpc, the cooling time becomes equal to the flow time and the wind can no longer cool efficiently; the thermal pressure of the post-shock material then accelerates the shell of swept-up gas to much greater velocities (for details of theoretical models see Supplementary Section 2).

Figure 2 shows how closely the observations qualitatively match the scenario described above. Indeed, the proposed scenario suggests that the gas entrained in the wind cools efficiently up to the acceleration point and maintains a constant or slightly decreasing velocity profile by dissipating the wind kinetic energy through radiation. On larger scales, the r^{-2} decrease of the AGN radiation energy density finally makes the cooling time longer than the flow time and the energy that is not radiated away causes a violent acceleration of the wind (see Supplementary Section 2 for details). Although the physical model is obviously oversimplified, in Fig. 2 we report three outflow velocity

Table 2 | Galaxy properties and best-fit parameters of the ionized outflows in the sample

Galaxy	Fit parameters										
	R_0 (kpc)*	$V_{r,\text{blue}}$ (km s $^{-1}$)	$V_{r,\text{red}}$ (km s $^{-1}$)	β_{blue} (°)	β_{red} (°)	θ (°)*	γ_{blue} (°)*	γ_{red} (°)*	N_{out}	β_{disk} (°)	$V_{\text{esc}}^{20\text{kpc}}$ (km s $^{-1}$)
NGC 4945	0.54	1,008 ± 41	930 ± 35	72 ± 4	101 ± 6	100	50	230	8 (4.4)	80 ± 9	240
Circinus	0.61	515 ± 38	—	74 ± 6	—	110	65	—	6 (5)	61 ± 8	400
NGC 7582	3.28	650 ± 52	645 ± 57	70 ± 4	112 ± 6	120	116	296	8 (4.4)	80 ± 8	300
Centaurus A	0.46	760 ± 52	730 ± 52	90 ± 6	93 ± 4	80	305	125	8 (3.1)	107 ± 4	240
NGC 1365	2.7	975 ± 35	620 ± 37	84 ± 8	92 ± 13	120	230	50	8 (4)	125 ± 7	365
NGC 2992	5.3	700 ± 37	710 ± 50	81 ± 7	120 ± 6	110	60	240	7 (3.1)	80 ± 7	310
IC 5063	6.5	775 ± 70	1110 ± 64	70 ± 7	110 ± 3	80	60	230	8 (3.1)	80 ± 4	380
NGC 5643	2.10	710 ± 57	770 ± 54	80 ± 3	86 ± 4	100	275	95	8 (3.1)	75 ± 8	190
NGC 5728	6.4	800 ± 42	890 ± 54	82 ± 3	100 ± 7	90	55	235	8 (2.2)	80 ± 5	370
IC 1657	4.8	710 ± 55	650 ± 48	86 ± 3	103 ± 4	100	94	274	8 (2.5)	102 ± 8	290

The asterisks indicate parameters that were kept fixed during the fitting procedure. The outflow extension (R_0), mean blueshifted and redshifted outflow radial velocity computed across all shells (that is, radii) ($\langle V_{r,\text{blue}} \rangle$ and $\langle V_{r,\text{red}} \rangle$, respectively), inclination with respect to the line of sight of (bi)conical outflows ($\beta_{\text{blue}}, \beta_{\text{red}}$), outer semi-aperture of the conical model (θ), position angle measured counterclockwise from north ($\gamma_{\text{blue}}, \gamma_{\text{red}}$), the number of concentric outflow shells (N_{out}), the shell width in arcsec is given in parentheses), mean inclination of the disk (β_{disk}) and wind velocity at radius R_0 to reach the 20 kpc scale ($V_{\text{esc}}^{20\text{kpc}}$; see 'Escape velocity' in the Methods) are listed for each source. Semi-apertures and position angles were fixed before the fit. The uncertainties on the free parameters were estimated by performing a fit of the emission integrated over R_0 with a wind opening angle of θ . Outflow radial velocity profiles for each source are shown in Fig. 2. For NGC2992, we adopted two different outflow radii: the redshifted and blueshifted cones had extensions of 35° and 20°, respectively.

profiles predicted by the theoretical model to highlight the striking similarities to the observed outflow properties, suggesting that this model is well suited to describing the physics behind the observed velocity profiles. The profiles were obtained by solving the equation of motion for the momentum- and energy-driven regimes of ref. 30 using three different stellar velocity dispersion values and $M_{\text{BH}} = 10^8 M_{\odot}$ (see also the caption of Fig. 2 and Supplementary Section 2).

Using MOKA^{3D} we were also able to fit and deproject the rotational velocity profile of the ionized gas in the galaxy disk and thus, following the prescription in ref. 31, compute the minimum velocity required for the outflowing gas to escape the host galaxy (see 'Escape velocity' in the Methods for a detailed discussion of the modelling of the galaxy potential using two different methodologies). Figure 3 shows the ratio between the outflow velocity and the escape velocity (V_{esc}) as a function of the distance from the nucleus. Shaded areas represent the ratio between the outflow and the velocity necessary to escape from the galaxy potential, reaching a 20 or 100 kpc radius.

For most sources, we found that the outflow radial velocity is consistently higher (by up to three times) than the escape velocity (for example, see NGC 4945 and Cen A) and thus the gas is free to escape at any radius. In NGC 7582, IC 1657 and IC 5063, the $V_{\text{out}}/V_{\text{esc}}$ ratio is slightly larger than unity up to a scale of 1 kpc, and then steeply increases through the acceleration of outer shells. Circinus shows a $V_{\text{out}}/V_{\text{esc}}$ ratio that slowly increases with radius, as the outflow velocity remains on average constant up to the edge of the field of view, while the escape velocity decreases with distance from the SMBH. Finally, we highlight the interesting velocity profiles of NGC 5728 and NGC 2992. For these two sources, the smooth deceleration of the outflow on the -1 kpc scale might prevent the gas being expelled, establishing a condition of $V_{\text{out}}/V_{\text{esc}} \leq 1$ for an extensive physical scale. The subsequent acceleration, presumably a result of the transition from a momentum- to an energy-driven phase, translates into a drastic increase of the ratio, making it possible for the gas to escape. The trend in Fig. 3 suggests that the gas entrained in the outflow can reach the galaxy outskirts, so AGN-powered galactic winds can cause feedback by expelling gas, playing a key role in regulating SMBH growth and star formation by sweeping the ambient gas out of the host potential.

As previously mentioned, AGN-driven outflows may have a crucial role in shaping galaxy properties and evolution and thus it is vital to carry out detailed studies to derive the intrinsic physical properties

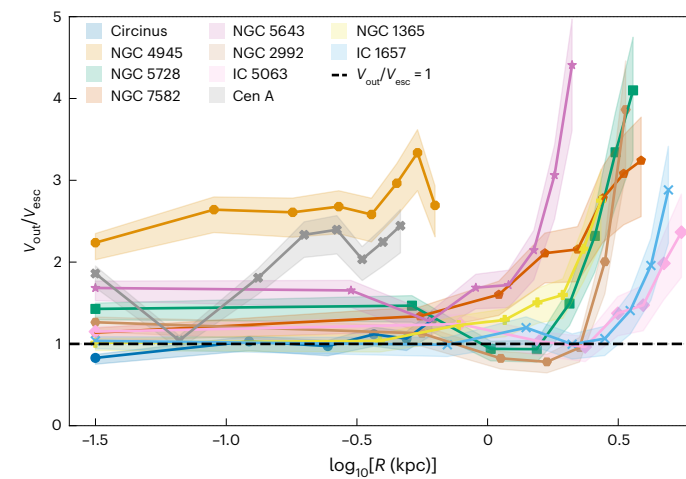


Fig. 3 | Ratio between the outflow intrinsic radial velocity and the host galaxy escape velocity as a function of the distance from the AGN. The dashed black line marks the ratio under which the outflowing gas is bounded by the host potential. The model used to compute the host potential, and thus the escape velocity at different radii, is discussed in 'Escape velocity' in the Methods. The shaded envelopes represent intervals of the escape velocity estimated for a particle to reach a maximum radius between 20 and 100 kpc using the equation presented in 'Escape velocity' in the Methods.

of outflows. In particular, characterizing the winds' kinematics and entrained mass is the first step to constrain the outflow kinetic power and thus the amount of energy transferred to the galaxy ISM. Comparing the outflow kinetic power to the AGN bolometric luminosity (L_{bol}) provides an estimate of the coupling efficiency factor between the wind and the AGN. While this comparison offers important insights into the potential impact of AGN-driven outflows on host evolution, it should be noted that systematic uncertainties still affect the kinetic coupling efficiency and thus linking such observationally derived coupling efficiencies to theoretical predictions is not straightforward^{8,15,23,32}. Energetic winds in particular can drastically influence star formation within the host galaxy by perturbing and expelling substantial amounts of gas out of it, possibly explaining the observed dearth of massive star-forming galaxies in the local Universe³³.

Our results highlight how crucial it is to achieve high intrinsic spatial resolution and analyse observations with accurate kinematic models to uncover the energy-driven phase of AGN winds. Indeed, the theoretically predicted energy-driven regime is established at distances ≥ 1 kpc, at which the intrinsic [O III] luminosity is much smaller than that in the circumnuclear region. This means that if both the momentum- and energy-driven regimes are established in an AGN outflow, the latter is harder to observe than the former because of the lower luminosity of the emitting gas at larger distances. In all our targets the non-detection of the fainter and more distant energy-driven regime could lead us to assume (incorrectly) much lower intrinsic outflow velocities. If this situation held at all redshifts, it would mean that only the brightest and slowest innermost shells of the outflow would normally be detected in high- z AGN. This would lead to underestimates of the intrinsic outflow velocities and thus the $V_{\text{out}}/V_{\text{esc}}$ ratios, with major consequences for the broad picture of galaxy evolution. Observational limitations, especially at high z , might therefore cause one to miss contributions to the feedback mechanism. We stress the need to obtain robust estimates of the ejected mass rates to specify the efficiency of this channel, and ultimately better understand the AGN feedback mechanism.

In this study we have provided a spatially resolved observational confirmation of the AGN outflow acceleration regime. Moreover, we demonstrate the importance of spatially resolved observations and a suitable model to interpret them. We see that the inefficiency of post-shock cooling is what leads to acceleration of the gas shell and pushes it out of the host potential^{34,35}. Our results for the behaviour of AGN winds conform closely to theoretical predictions of expanding bubbles, and represent a major step forwards in understanding phenomena such as AGN feedback and the mechanism powering it, and the co-evolution of SMBHs and their hosts (for example, successful applications of MOKA^{3D} for deriving AGN-driven outflow properties both at low and high z are presented in refs. 36–38). These results also improve our understanding of the impact of outflows on the ISM. In future work, we will apply our model to several other low- and high- z galaxies with the aim of providing key insights into the intrinsic properties of outflows in different environmental conditions.

Methods

Observations and spectroscopic analysis

The galaxies in our sample were observed by the optical integral field spectrograph Multi Unit Spectroscopic Explorer (MUSE; ref. 39) at the Very Large Telescope in wide-field mode. The data consist of data cubes with two spatial and one spectral extension. We analysed each data cube by means of a set of custom Python scripts to first subtract the stellar continuum and then fit multiple Gaussian components to the emission lines, thus finally obtaining an emission-line model cube for each emission line of interest. For a more detailed description of the data reduction and spectroscopic analysis we refer the reader to refs. 16,40,41. To map outflow properties, we used the [O III] $\lambda 5007$ and [N II] $\lambda 6584$ emission lines. They are both optimal tracers of the ionized phase of outflows on 10^2 – 10^3 -pc scales, as they can only be produced in low-density regions and therefore do not trace the sub-parsec scales of the broad line region.

We created moment maps of the ionized emission from the cube fit: the integrated line flux (moment of order 0), the flux-weighted line-of-sight velocity (moment of order 1) and the velocity dispersion maps (moment of order 2). See the top panels in Fig. 1 and Supplementary Figs. 4–6 for the observed moment maps of our sample. These maps are fundamental to provide a first hint of the ionized gas kinematics and morphology to be used as a starting point for the modelling with MOKA^{3D}. As stressed in ref. 24, the ability of a given kinematic model to reproduce the observed moment maps does not guarantee that the derived properties are a faithful representation of the features and physical properties of outflows due to the high level of degeneracy

affecting this kind of analysis, and thus more accurate line profile modelling is needed (see section 2.6 in ref. 24 for a detailed discussion on outflow kinematic degeneracies).

Target selection

Our sample comprised ten nearby AGN from the MAGNUM survey. These sources were selected by cross-matching the optically selected AGN samples of ref. 42 and ref. 43 and the Swift-BAT 70-month Hard X-ray Survey⁴⁴, choosing only sources observable from Paranal Observatory ($-70^\circ < \delta < 20^\circ$) and with a luminosity distance $D_L \leq 50$ Mpc. The distances and M_{BH} values of the galaxies in our sample are listed in Table 1. In total, the MAGNUM sample collects ~80 sources, of which we selected those that show a well-shaped (bi)conical outflow emission traced by [O III] $\lambda 5007$ or [N II] $\lambda 6584$ emission lines. Moreover, we decided to select sources that span the widest possible range of distances (that is, from NGC 4945 (~3.7 Mpc) to IC 1657 (~50 Mpc)) with outflows on scales from ~500 pc in Cen A and NGC 4945 up to ~5 kpc in IC 5063. As a consequence of their vicinity and high spatial resolution in MUSE data, all sources showed clumpy ionized gas distributions, which was not a selection criterion. In order of distance, the sample comprises: NGC 4945, Cen A, Circinus, NGC 5643, NGC 1365, NGC 7582, NGC 2992, NGC 5728, IC 5063 and IC 1657 (refs. 16,24–26,45).

Data modelling with MOKA^{3D}

To model and interpret the kinematics of line emission, we adopted the innovative tool MOKA^{3D} presented in ref. 24. MOKA^{3D} is a 3D kinematic model that assumes a spherical or cylindrical geometry populated with a 3D distribution of emitting clouds. These clouds are weighted according to the observed line flux in each spaxel and spectral channel of the data cube. The outflow clouds follow a simple radial velocity field that is free to vary with radius and is based on the chosen geometry and the cloud position in the 3D space. We improved the routine presented in ref. 24 by implementing a more sophisticated fitting procedure. In particular, in this updated version we reproduced the spatially resolved gas properties as a function of the distance from the nucleus, instead of fitting the spatially averaged properties of the outflow. For some sources in our sample it was difficult to constrain the outflow morphology due to its superposition with the galaxy disk in projection (for example NGC 5643, IC 1657 and NGC 1365). Therefore, we combined two kinematic components (outflow + disk) to model the total emission and best reproduce the observed features. We modelled the outflow with a biconical, spherically symmetric model and the disk as a cylindrically symmetric model. In our routine, we fitted the gas properties by dividing the outflow and the disk in concentric shells of fixed width. The number of shells, and thus their intrinsic width, was tailored to the outflow size in each source to minimize their overlap once projected on the plane of the sky. There were two free model parameters in each shell: the outflow (disk) intrinsic radial (rotational) velocity and inclination with respect to the line of sight. First, we masked the outflow spatial shape in the observed moment maps and fitted the rotating gas disk emission in concentric annuli of fixed width (with the rotational velocity and inclination of each annulus set as free parameters) and were able to reproduce the observed ionized emission in the galaxy disk. We then created a separate model cube for the outflow, assuming that the model clouds follow a radial motion (see equation (3) in ref. 24) and combined it with the disk model cube. As discussed in ref. 24, to fit the outflow emission in each source we fixed the position angle (y), the conical aperture of the outflow and the centre of the outflow model, as they are parameters that can be constrained from observations. To infer the centre of the outflow model we collapsed the total [O III] $\lambda 5007$ emission and performed a 2D Gaussian fit to the collapsed image. For the unusual case of Cen A, which has a highly obscured nucleus, we measured the centre position from the intersect of the major and minor disk axes. We fixed the outer aperture of the conical model by measuring the minimum angle that enclosed the observed conical

ionized emission. Then, we fixed the position angle by measuring the bisectrix of the conical model starting from the measured centre. Finally, we fitted the outflow emission in each shell, while keeping the underlying rotating disk fixed with the best-fit properties derived from the previous fit, aiming to infer only the properties of the disk. To do this, we compared the observed and modelled spectra shell by shell. In particular, we compared the observed and modelled percentile velocities at 1% and 99% of the emission line integrated over each conical shell, requiring that they differed by no more than 5%. The free parameters in each shell were the intrinsic velocity and the inclination with respect to the line of sight. As a result, we obtained the velocity and inclination as a function of the distance from the nucleus for each shell of each model (see Supplementary Section 1 and Supplementary Fig. 1). As previously outlined, the disk and outflow emission were fitted by two independent procedures for each galaxy. Therefore, for each individual fit, the total number of free parameters was two (that is, the velocity and inclination; Table 2). A detailed discussion of the MOKA^{3D} goodness-of-fit estimator used to infer the best-fit parameters, as well as the procedure to estimate the parameter uncertainties, is presented in Supplementary Section 3. In Supplementary Figs. 4–6 we show the observed, modelled and residual moment maps for each source in our sample. The intensity maps (top left for each source in Supplementary Figs. 4–6) show a clear biconical axis-symmetric geometry for each source except Circinus, where the counter cone is probably obscured by the galactic disk⁴⁶. For all cases except NGC 5728 and IC 1657, the redshifted cone is more obscured by dust than the approaching cone, as expected in Seyfert galaxies with axis-symmetric conical winds, as the counter cone is typically partially or totally hidden by the galaxy disk (for example, see ref. 16). To fit the emission of the ionized gas in the disk, we adopted a thin disk geometry with a disk width of 1'' for each source, without including any intrinsic velocity dispersion for the disk clouds. As a consequence, just a few clouds of the disk model will fall in each spaxel and thus we expect higher residuals from the disk-dominated region than from the outflow-dominated spaxels. This effect can be ascribed to the choice to model the emission from the disk with a thin disk geometry, which does not account for non-circular motions and deviations from the simple disk geometry (as disk bulges or thick clumps that deviate from the thin disk geometry).

MOKA^{3D} reproduces both the clumpy ionized emission and complex observed velocity fields, demonstrating that the observed complexity can be ascribed to the clumpy medium and not to the velocity field, which can be modelled with a smooth velocity function. It is worth noting that such complexity cannot be reproduced by assuming analytical flux functions, which cannot account for the clumpy ISM morphology (for example, refs. 21,22,47–49). We found that the effect of increased velocity dispersions perpendicular to biconical outflows in NGC 5643, NGC 5728 and IC 5063 (see⁵⁰ for a tentative explanation) was not well reproduced with MOKA^{3D}. These features trace an enhancement of the turbulence in the ISM, which may be due to the interaction with the radio jet and thus cannot be reproduced by our outflow + disk model. However, this feature does not affect our modelling of the outflow properties. It is important to stress that the underlying disk emission is negligible when the goal is to model and reproduce the intrinsic outflow properties, as the disk emission is limited to small velocities which do not affect the high-velocity tails of the line profile. Indeed, in our MAGNUM sample we measured average rotating disk velocities ranging from a few tens of kilometres per second in the inner shells up to ~250 km s⁻¹ in the outer regions. Such velocities are considerably smaller than the intrinsic outflow velocities at each radius and thus would not affect our results.

MOKA^{3D} fitting and outflow velocity

Our results for the intrinsic outflow average velocity were generally consistent with previous kinematic analyses (see the average velocities listed in Table 2). In particular, we compared the results for Circinus,

NGC 4945 and NGC 7582 with our previous analysis in ref. 24, where we fitted the data for each source, imposing a constant and average outflow velocity and inclination. Here we demonstrated that a constant outflow velocity still provides the optimal fit for Circinus and NGC 4945 up to the observed scales. In particular, in ref. 24 the outflow properties of Circinus and NGC 4945 were reasonably well reproduced with cone axis inclinations of $\beta = 80 \pm 2^\circ$ and $\beta = 70 \pm 5^\circ$ and constant outflow velocities of $V_r = 550 \pm 20$ km s⁻¹ and $V_r = 1,200 \pm 50$ km s⁻¹, respectively. In this work, we found $\beta = 75 \pm 5^\circ$ and $\beta = 72 \pm 7^\circ$ and $V_r = 517 \pm 37$ km s⁻¹ and $V_r = 1,010 \pm 90$ km s⁻¹ for Circinus and NGC 4945, respectively. The mentioned average outflow properties presented here were estimated by computing the mean and standard deviation of the best-fit values in the various conical shells, as reported in Fig. 2. On average, the outflow properties reported in ref. 24 and in this work for Circinus and NGC 4945 are consistent. For NGC 7582, to quantify the improvements with respect to our previous analysis and to demonstrate that an accelerating velocity profile is better suited to reproduce the observed features of this source, we compared the goodness-of-fit estimator (κ) for the new best-fit model and the one presented in ref. 24. We found that our new routine improved the fitting by a factor of ~2; that is $\kappa_{\text{acc}}/\kappa_{\text{const}} = 0.42$, where κ_{acc} and κ_{const} are revised from the κ presented in ref. 24 for the accelerating and constant velocity models, respectively. A detailed discussion of κ , as well as the procedure used to derive the best-fit parameter uncertainties, is presented in Supplementary Section 3. Finally, we discuss the nature of the discrepancies in the best-fit values derived in this work with respect to those presented in ref. 24. With our improved tool we found $\beta = 71 \pm 5^\circ$ and $V_r = 660 \pm 150$ km s⁻¹, whereas ref. 24 reported $\beta = 88 \pm 2^\circ$ and $V_r = 630 \pm 30$ km s⁻¹. We found that the estimates of the radial velocity provided with the two methods are consistent within the uncertainties. However, in this work we found an outflow axis that is more inclined towards the observer with respect to that provided in ref. 24. Nevertheless, since in this work we also accounted for the emission originating from the underlying disk and performed an estimate of the radial profile of the outflow inclination (which showed consistency among the different shells; top panel of Supplementary Fig. 1), we believe that the result provided here is more reliable. Consistent with our averaged result, ref. 51 and ref. 52 studied the same MUSE wide-field-mode data for Circinus and assumed outflow velocities of ~750 km s⁻¹ and 400 km s⁻¹, respectively, derived from [O III] channel maps and from the full-width at half-maximum of the broad [O III] component, respectively. For NGC 4945 and NGC 1365, ref. 53 found ionized outflow velocities of 800 km s⁻¹ and 500 km s⁻¹, respectively, using the difference between the velocities at the 85th and at the 15th percentile of the total fitted profile (W_{70}) as a proxy of outflow velocity. Previous studies failed to address the properties of the ionized gas of the outflow in Cen A. Ref. 54 and ref. 55 traced the outflow velocity in NGC 5728 and found maximum values of 400 km s⁻¹ and 740 km s⁻¹ from Pa β and [Si VI] emission, respectively. Reference 45 confirmed ionized outflow velocities above 1,000 km s⁻¹ in NGC 2992, consistent with our results and in contrast with previous analyses (for example, ref. 56). In NGC 5643, ref. 57 and ref. 25 found outflow velocities up to 700 km s⁻¹ and 450 km s⁻¹, respectively. In the latter, the outflow velocity was measured as the velocity at 10% of the [O III] line flux. Taking into account projection effects and considering all of the line profile, both of these estimates are consistent with our results. An estimate of the ionized outflow velocity in IC 1656 is provided in ref. 52, which used the nonparametric velocity dispersion w_{80} from slit spectra as a proxy of outflow velocity and found velocities of ~400 km s⁻¹, which is below our spatially resolved estimate. Lastly, ref. 58 projected ionized flux-weighted maximum outflow velocities of ~300 km s⁻¹ in NGC 7582, which is not consistent with our results even when deprojecting the outflow velocity. One possible reason for this inconsistency might be that they were observing the flux-weighted gas velocity and thus not taking into account the contribution from the gas producing the fainter line wings, which would lead them to assume a higher outflow velocity.

Escape velocity

We computed the escape velocity profiles for all our MAGNUM galaxies using two different methodologies. First, based on the prescription of ref. 31, we assumed a spherically symmetric galaxy and modelled the potential as in a singular isothermal truncated sphere (to avoid the mass to diverge we truncated the sphere at the halo radius; that is, $R_{\max} = R_{\text{halo}}$). Then, to obtain estimates as conservative as possible, we used the maximum disk velocity measured with MOKA^{3D} as the disk velocity (V_{rot}). Finally, we could then describe the escape velocity as: $V_{\text{esc}}(r) = V_{\text{rot}} \sqrt{2(1 + \ln(R_{\max}/r))}$, where r is the distance from the AGN. The second method to estimate the escape velocity profile was based on ref. 59. In brief, we built a dynamical mass model using the galpy⁶⁰ Python package and derived the total rotation curves and escape velocity curves. Our mass model consisted of a dark-matter halo, a stellar disk and a gaseous disk. We modelled the dark-matter halo using an NFW profile, deriving its virial mass M_{200} and concentration c from the stellar-to-halo mass relation of ref. 61 and the M_{200} – c relation of ref. 62, respectively. For the stellar disk, we assumed a double-exponential profile with scale length R_d and scale-height $R_d/5$, where R_d is equal to the half-light radius R_{50} divided by 1.68 (correct for a pure exponential disk, Sérsic index $n = 1$). We determined R_{50} from the size– M -relation for a disk galaxy ($n = 1$) at $z \approx 0$ (ref. 63) adopting the stellar masses listed in Table 1. We modelled a gaseous disk with M_{gas} adopting the values listed in Table 1. In doing so, we derived the escape velocity profile of the total mass distribution. Despite the differences in assumptions between the two methods, we derived consistent values for the escape velocity profile. Given that both models are well suited to computing the escape velocity in our sample, we decided to adopt the estimates from the first model as it is simpler and does not rely on measurements of galactic properties (such as M , M_{gas} and M_{BH}) to set the galaxy dynamics.

Data availability

All data are public and available on the ESO archive processed data portal at <https://archive.eso.org/scienceportal/home>.

References

1. Tombesi, F. et al. Evidence for ultra-fast outflows in radio-quiet AGNs. I. Detection and statistical incidence of Fe K-shell absorption lines. *Astron. Astrophys.* **521**, A57 (2010).
2. Sturm, E. et al. Massive molecular outflows and negative feedback in ULIRGs observed by Herschel-PACS. *Mon. Not. R. Astron. Soc.* **733**, L16 (2011).
3. Cicone, C. et al. Massive molecular outflows and evidence for AGN feedback from CO observations. *Astron. Astrophys.* **562**, A21 (2014).
4. Cresci, G. et al. Blowin' in the wind: both negative and positive feedback in an obscured high quasar. *Astrophys. J.* **799**, 82 (2015).
5. Carniani, S. et al. Ionised outflows in $z \sim 2.4$ quasar host galaxies. *Astron. Astrophys.* **580**, A102 (2015).
6. Carniani, S. et al. Fast outflows and star formation quenching in quasar host galaxies. *Astron. Astrophys.* **591**, A28 (2016).
7. Cicone, C. et al. The largely unconstrained multiphase nature of outflows in AGN host galaxies. *Nat. Astron.* **2**, 176–178 (2018).
8. Harrison, C. M. et al. AGN outflows and feedback twenty years on. *Nat. Astron.* **2**, 198–205 (2018).
9. Fluetsch, A. et al. Cold molecular outflows in the local Universe and their feedback effect on galaxies. *Mon. Not. R. Astron. Soc.* **483**, 4586–4614 (2019).
10. Pérez-González, P. G. et al. The stellar mass assembly of galaxies from $z = 0$ to $z = 4$: analysis of a sample selected in the rest-frame near-infrared with Spitzer. *Astrophys. J.* **675**, 234–261 (2008).
11. Fabian, A. C. Observational evidence of active galactic nuclei feedback. *Annu. Rev. Astron. Astrophys.* **50**, 455–489 (2012).
12. Zubovas, K. & King, A. Clearing out a galaxy. *Astrophys. J. Lett.* **745**, L34 (2012).
13. Cresci, G. & Maiolino, R. Observing positive and negative AGN feedback. *Nat. Astron.* **2**, 179–180 (2018).
14. Cano-Díaz, M. et al. Observational evidence of quasar feedback quenching star formation at high redshift. *Astron. Astrophys.* **537**, L8 (2012).
15. Harrison, C. M., Alexander, D. M., Mullaney, J. R. & Swinbank, A. M. Kiloparsec-scale outflows are prevalent among luminous AGN: outflows and feedback in the context of the overall AGN population. *Mon. Not. R. Astron. Soc.* **441**, 3306–3347 (2014).
16. Mingozi, M. et al. The MAGNUM survey: different gas properties in the outflowing and disc components in nearby active galaxies with MUSE. *Astron. Astrophys.* **622**, A146 (2019).
17. Kakkad, D. et al. Dissecting the active galactic nucleus in Circinus – IV. MUSE-NFM observations unveil a tuning-fork ionized outflow morphology. *Mon. Not. R. Astron. Soc.* **519**, 5324–5332 (2023).
18. Speranza, G. et al. Multiphase characterization of AGN winds in five local type-2 quasars. *Astron. Astrophys.* **681**, A63 (2024).
19. Chu, B. R. et al. DUVET: sub-kiloparsec resolved star formation driven outflows in a sample of local starbursting disk galaxies. *Mon. Not. R. Astron. Soc.* **536**, 1799–1821 (2025).
20. Lai, T. S.-Y. et al. GOALS-JWST: tracing AGN feedback on the star-forming interstellar medium in NGC 7469. *Astrophys. J. Lett.* **941**, L36 (2022).
21. Crenshaw, D. M. et al. A kinematic model for the narrow-line region in NGC 4151. *Astron. J.* **120**, 1731–1738 (2000).
22. Das, V. et al. Mapping the kinematics of the narrow-line region in the Seyfert galaxy NGC 4151. *Astron. J.* **130**, 945–956 (2005).
23. Storchi-Bergmann, T. et al. Feeding versus feedback in NGC 4151 probed with Gemini NIFS – I. Excitation. *Mon. Not. R. Astron. Soc.* **394**, 1148–1166 (2009).
24. Marconcini, C. et al. MOKA^{3D}: an innovative approach to 3D gas kinematic modelling. I. Application to AGN ionised outflows. *Astron. Astrophys.* **677**, A58 (2023).
25. Cresci, G. et al. The MAGNUM survey: positive feedback in the nuclear region of NGC 5643 suggested by MUSE. *Astron. Astrophys.* **582**, A63 (2015).
26. Venturi, G. et al. MAGNUM survey: a MUSE-Chandra resolved view on ionized outflows and photoionization in the Seyfert galaxy NGC1365. *Astron. Astrophys.* **619**, A74 (2018).
27. King, A. Black holes, galaxy formation, and the $M_{\text{BH}}-\sigma$ relation. *Astrophys. J. Lett.* **596**, L27–L29 (2003).
28. Ciotti, L. & Ostriker, J. P. Cooling flows and quasars: different aspects of the same phenomenon? I. Concepts. *Mon. Not. R. Astron. Soc. Lett.* **487**, L105–L108 (1997).
29. King, A. R., Zubovas, K. & Power, C. Large-scale outflows in galaxies. *Mon. Not. R. Astron. Soc.* **415**, L6–L10 (2011).
30. King, A. R. & Pounds, K. A. Black hole winds. *Mon. Not. R. Astron. Soc.* **345**, 657–659 (2003).
31. Veilleux, S., Maiolino, R., Bolatto, A. D. & Aalto, S. Cool outflows in galaxies and their implications. *Astron. Astrophys. Rev.* **28**, 2 (2020).
32. Feruglio, C. et al. The multi-phase winds of Markarian 231: from the hot, nuclear, ultra-fast wind to the galaxy-scale, molecular outflow. *Astron. Astrophys.* **583**, A99 (2015).
33. Di Matteo, T., Springel, V. & Hernquist, L. Energy input from quasars regulates the growth and activity of black holes and their host galaxies. *Nature* **433**, 604–607 (2005).
34. Manzano-King, C. M., Canalizo, G. & Sales, L. V. AGN-driven outflows in dwarf galaxies. *Astrophys. J.* **884**, 54 (2019).
35. Smethurst, R. J. et al. Kiloparsec-scale AGN outflows and feedback in merger-free galaxies. *Mon. Not. R. Astron. Soc.* **507**, 3985–3997 (2021).

36. Cresci, G. et al. Bubbles and outflows: the novel JWST/NIRSpec view of the $z=1.59$ obscured quasar XID2028. *Astron. Astrophys.* **672**, A128 (2023).

37. Perna, M. et al. GA-NIFS: a galaxy-wide outflow in a Compton-thick mini-BAL quasar at $z=3.5$ probed in emission and absorption. *Astron. Astrophys.* **694**, A170 (2025).

38. Ulivi, L. et al. JWST/NIRSpec insights into the circumnuclear region of Arp 220: a detailed kinematic study. *Astron. Astrophys.* **693**, A36 (2025).

39. Bacon, R. et al. The MUSE second-generation VLT instrument. *Proc. SPIE* **7735**, 773508 (2010).

40. Marasco, A. et al. Galaxy-scale ionised winds driven by ultra-fast outflows in two nearby quasars. *Astron. Astrophys.* **644**, A15 (2020).

41. Tozzi, G. et al. Connecting X-ray nuclear winds with galaxy-scale ionised outflows in two $z \sim 1.5$ lensed quasars. *Astron. Astrophys.* **648**, A99 (2021).

42. Maiolino, R. & Rieke, G. H. Low-luminosity and obscured Seyfert nuclei in nearby galaxies. *Astrophys. J.* **454**, 95 (1995).

43. Risaliti, G., Maiolino, R. & Salvati, M. The distribution of absorbing column densities among Seyfert 2 galaxies. *Astrophys. J.* **522**, 157–164 (1999).

44. Baumgartner, W. H. et al. The 70 month Swift-BAT all-sky hard X-ray survey. *Astrophys. J. Suppl. Ser.* **207**, 19 (2013).

45. Zanchettin, M. V. et al. NGC 2992: interplay between the multiphase disc, wind, and radio bubbles. *Astron. Astrophys.* **679**, A88 (2023).

46. Elmouttie, M., Haynes, R. F., Jones, K. L., Sadler, E. M. & Ehle, M. Radio continuum evidence for nuclear outflow in the Circinus galaxy. *Mon. Not. R. Astron. Soc.* **297**, 1202–1218 (1998).

47. Fischer, T. C. et al. Modeling the outflow in the narrow-line region of Markarian 573: biconical illumination of a gaseous disk. *Astron. J.* **140**, 577–583 (2010).

48. Müller-Sánchez, F. et al. Outflows from active galactic nuclei: kinematics of the narrow-line and coronal-line regions in Seyfert galaxies. *Astrophys. J.* **739**, 69 (2011).

49. Bae, H.-J. & Woo, J.-H. The prevalence of gas outflows in type 2 AGNs. II. 3D biconical outflow models. *Astrophys. J.* **828**, 97 (2016).

50. Venturi, G. et al. MAGNUM survey: compact jets causing large turmoil in galaxies. Enhanced line widths perpendicular to radio jets as tracers of jet-ISM interaction. *Astron. Astrophys.* **648**, A17 (2021).

51. Fonseca-Faria, M. A., Rodríguez-Ardila, A., Contini, M. & Reynaldi, V. The ionized gas outflow in the Circinus galaxy: kinematics and physical conditions. *Mon. Not. R. Astron. Soc.* **506**, 3831–3852 (2021).

52. Kakkad, D. et al. BASS XXXI: outflow scaling relations in low redshift X-ray AGN host galaxies with MUSE. *Mon. Not. R. Astron. Soc.* **511**, 2105–2124 (2022).

53. Venturi, G. et al. Ionized gas outflows from the MAGNUM survey: NGC 1365 and NGC 4945. *Front. Astron. Space Sci.* **4**, 46 (2017).

54. Durré, M. & Mould, J. The AGN ionization cones of NGC 5728. II. Kinematics. *Astrophys. J.* **870**, 37 (2019).

55. Shimizu, T. T. et al. The multiphase gas structure and kinematics in the circumnuclear region of NGC 5728. *Mon. Not. R. Astron. Soc.* **490**, 5860–5887 (2019).

56. Guolo-Pereira, M. et al. Exploring the AGN-merger connection in Arp 245 I: nuclear star formation and gas outflow in NGC 2992. *Mon. Not. R. Astron. Soc.* **502**, 3618–3637 (2021).

57. García-Bernete, I. et al. Multiphase feedback processes in the Sy2 galaxy NGC 5643. *Astron. Astrophys.* **645**, A21 (2021).

58. Juneau, S. et al. The black hole–galaxy connection: interplay between feedback, obscuration, and host galaxy substructure. *Astrophys. J.* **925**, 203 (2022).

59. Tozzi, G. et al. SUPER VIII. Fast and furious at $z \sim 2$: obscured type-2 active nuclei host faster ionised winds than type-1 systems. *Astron. Astrophys.* **690**, A141 (2024).

60. Bovy, J. galpy: a python library for galactic dynamics. *Astrophys. J. Suppl. Ser.* **216**, 29 (2015).

61. Girelli, G. et al. The stellar-to-halo mass relation over the past 12 Gyr. I. Standard Λ CDM model. *Astron. Astrophys.* **634**, A135 (2020).

62. Dutton, A. A. & Macciò, A. V. Cold dark matter haloes in the Planck era: evolution of structural parameters for Einasto and NFW profiles. *Mon. Not. R. Astron. Soc.* **441**, 3359–3374 (2014).

63. Mowla, L., van der Wel, A., van Dokkum, P. & Miller, T. B. A mass-dependent slope of the galaxy size–mass relation out to $z \sim 3$: further evidence for a direct relation between median galaxy size and median halo mass. *Astrophys. J. Lett.* **872**, L13 (2019).

64. Greenhill, L. J., Moran, J. M. & Herrnstein, J. R. The distribution of H₂O maser emission in the nucleus of NGC 4945. *Mon. Not. R. Astron. Soc. Lett.* **481**, L23–L26 (1997).

65. Davis, B. L. et al. The black hole mass function derived from local spiral galaxies. *Astrophys. J.* **789**, 124 (2014).

66. Wold, M., Lacy, M., Käufl, H. U. & Siebenmorgen, R. The nuclear regions of NGC 7582 from [Ne II] spectroscopy at 12.8 μm – an estimate of the black hole mass. *Astron. Astrophys.* **460**, 449–457 (2006).

67. Cappellari, M. et al. The mass of the black hole in Centaurus A from SINFONI AO-assisted integral-field observations of stellar kinematics. *Mon. Not. R. Astron. Soc.* **394**, 660–674 (2009).

68. Caglar, T. et al. LLAMA: the $M_{\text{BH}}-\sigma_*$ relation of the most luminous local AGNs. *Astron. Astrophys.* **634**, A114 (2020).

69. Goulding, A. D., Alexander, D. M., Lehmer, B. D. & Mullaney, J. R. Towards a complete census of active galactic nuclei in nearby galaxies: the incidence of growing black holes. *Mon. Not. R. Astron. Soc.* **406**, 597–611 (2010).

70. López-Cobá, C. et al. The AMUSING++ nearby galaxy compilation. I. Full sample characterization and galactic-scale outflow selection. *Astron. J.* **159**, 167 (2020).

71. For, B.-Q., Koribalski, B. S. & Jarrett, T. H. Gas and star formation in the Circinus galaxy. *Mon. Not. R. Astron. Soc.* **425**, 1934–1950 (2012).

72. Koss, M. J. et al. BAT AGN spectroscopic survey. XX. Molecular gas in nearby hard-X-ray-selected AGN galaxies. *Astrophys. J. Suppl. Ser.* **252**, 29 (2021).

73. Dahlem, M. et al. The distribution of CO in NGC 4945. *Astron. Astrophys.* **270**, 29–42 (1993).

74. Dahlem, M. Intergalactic neutral hydrogen gas in the Grus quartet of galaxies. *Astron. Astrophys.* **429**, L5–L8 (2005).

75. Parkin, T. J. et al. The gas-to-dust mass ratio of Centaurus A as seen by Herschel. *Mon. Not. R. Astron. Soc.* **422**, 2291–2301 (2012).

76. Lianou, S., Barmby, P., Mosenkov, A. A., Lehnert, M. & Karczewski, O. Dust properties and star formation of approximately a thousand local galaxies. *Astron. Astrophys.* **631**, A38 (2019).

77. Jorsater, S. & van Moorsel, G. A. High resolution neutral hydrogen observations of the barred spiral galaxy NGC 1365. *Astron. J.* **110**, 2037 (1995).

78. Morganti, R. et al. The fast molecular outflow in the Seyfert galaxy IC 5063 as seen by ALMA. *Astron. Astrophys.* **580**, A1 (2015).

Acknowledgements

C.M., G.C., A.M., F.M., F.B., E.B. and G.V. acknowledge the support of the INAF Large Grant 2022 ‘The metal circle: a new sharp view of the baryon cycle up to Cosmic Dawn with the latest generation IFU facilities’. C.M., G.C., A.M., G.T., F.M., F.B. and E.B. also acknowledge the support of grant number PRIN-MUR 2020ACSP5K_002 financed by the European Union–Next Generation EU. E.D.T. is supported by the European Research Council (ERC) under grant agreement number

101040751. A.M., F.M. and G.C. acknowledge support from the PRIN-MUR project 'PROMETEUS' financed by the European Union–Next Generation EU Mission 4 Component 1 CUP B53D23004750006. S.C. and G.V. acknowledge funding from the European Union (ERC, WINGS, grant number 101040227). G.T. acknowledges financial support from the ERC Advanced Grant under the European Union's Horizon Europe research and innovation programme (grant agreement AdG GALPHYS, number 101055023).

Author contributions

C.M. and A.M. designed and coordinated the work, prepared the figures and drafted the manuscript. All authors contributed to the analysis and interpretation of the data, the results and the final text.

Competing interests

The authors declare no competing interests.

Additional information

Supplementary information The online version contains supplementary material available at <https://doi.org/10.1038/s41550-025-02518-6>.

Correspondence and requests for materials should be addressed to Cosimo Marconcini.

Peer review information *Nature Astronomy* thanks Vincenzo Mainieri and the other, anonymous, reviewer(s) for their contribution to the peer review of this work.

Reprints and permissions information is available at www.nature.com/reprints.

Publisher's note Springer Nature remains neutral with regard to jurisdictional claims in published maps and institutional affiliations.

Springer Nature or its licensor (e.g. a society or other partner) holds exclusive rights to this article under a publishing agreement with the author(s) or other rightsholder(s); author self-archiving of the accepted manuscript version of this article is solely governed by the terms of such publishing agreement and applicable law.

© The Author(s), under exclusive licence to Springer Nature Limited 2025

¹Dipartimento di Fisica e Astronomia, Università degli Studi di Firenze, Firenze, Italy. ²INAF–Osservatorio Astrofisico di Arcetri, Firenze, Italy. ³University of Trento, Trento, Italy. ⁴Scuola Normale Superiore, Pisa, Italy. ⁵Max-Planck-Institut für Extraterrestrische Physik (MPE), Garching, Germany. ⁶School of Physics & Astronomy, University of Leicester, Leicester, UK. ⁷Astronomical Institute Anton Pannekoek, University of Amsterdam, Amsterdam, the Netherlands. ⁸Leiden Observatory, Leiden University, Leiden, the Netherlands.  e-mail: cosimo.marconcini@unifi.it